Editors' Suggestion

# Spin-orbital order and excitons in magnetoresistive HoBi

J. Gaudet,[1,2,3,*] H.-Y. Yang,[4] E. M. Smith,[5] T. Halloran,[1] J. P. Clancy,[5] J. A. Rodriguez-Rivera,[2,3] Guangyong Xu,[2] Y. Zhao,[2,3] W. C. Chen,[2] G. Sala,[6] A. A. Aczel,[7] B. D. Gaulin,[5,8,9] F. Tafti,[4] and C. Broholm[1,2,10]

[1]*Institute for Quantum Matter and Department of Physics and Astronomy, Johns Hopkins University, Baltimore, Maryland 21218, USA*
[2]*NIST Center for Neutron Research, National Institute of Standards and Technology, Gaithersburg, Maryland 20899, USA*
[3]*Department of Materials Science and Engineering, University of Maryland, College Park, Maryland 20742-2115, USA*
[4]*Department of Physics, Boston College, Chestnut Hill, Massachusetts 02467, USA*
[5]*Department of Physics and Astronomy, McMaster University, Hamilton, Ontario, Canada L8S 4M1*
[6]*Spallation Neutron Source, Second Target Station, Oak Ridge National Laboratory, Oak Ridge, Tennessee 37831, USA*
[7]*Neutron Scattering Division, Oak Ridge National Laboratory, Oak Ridge, Tennessee 37831, USA*
[8]*Canadian Institute for Advanced Research, 661 University Avenue, Toronto, Ontario, Canada M5G 1M1*
[9]*Brockhouse Institute for Materials Research, Hamilton, Ontario, Canada L8S 4M1*
[10]*Department of Materials Science and Engineering, The Johns Hopkins University, Baltimore, Maryland 21218, USA*

(Received 12 January 2023; accepted 6 March 2023; published 22 March 2023)

The magnetism of the rocksalt fcc rare-earth monopnictide HoBi, a candidate topological material with extreme magnetoresistance, is investigated. From the $Ho^{3+}$ non-Kramers $J = 8$ spin-orbital multiplet, the cubic crystal electric field yields six nearly degenerate low-energy levels. These constitute an anisotropic magnetic moment with a Jahn-Teller-like coupling to the lattice. In the cubic phase for $T > T_N = 5.72(1)$ K, the paramagnetic neutron scattering is centered at $\mathbf{k} = (\frac{1}{2}\frac{1}{2}\frac{1}{2})$ and was fit to dominant antiferromagnetic interactions between Ho spins separated by {100} and ferromagnetic interactions between spins displaced by $\{\frac{1}{2}\frac{1}{2}0\}$. For $T < T_N$, a type-II AFM long-range order with $\mathbf{k} = (\frac{1}{2}\frac{1}{2}\frac{1}{2})$ develops along with a tetragonal lattice distortion. While neutron diffraction from a multidomain sample cannot unambiguously determine the spin orientation within a domain, the bulk magnetization, structural distortion, and our measurements of the magnetic excitations all show the easy axis coincides with the tetragonal axis. The weakly dispersive excitons for $T < T_N$ can be accounted for by a spin Hamiltonian that includes the crystal electric field and exchange interactions within the random phase approximation.

DOI: 10.1103/PhysRevB.107.104423

## I. INTRODUCTION

In spite of their structural simplicity, the fcc rare-earth monopnictides (see Fig. 1), RX (R = Ce to Yb and X = N, As, P, Sb, and Bi [1,2]), display a wide variety of anisotropic magnetism and electronic transport properties. The lattice parameter varies by 30% across the pnictide series and this provides opportunities to tune the relative strength of crystal field and exchange interactions. In the 1960s to 1980s, the rare-earth monopnictides were studied to understand magnetic phases driven by oscillatory and highly anisotropic Ruderman-Kittel-Kasuya-Yosida (RKKY) exchange interactions [3–8]. Work on CeSb for example gave rise to an extensive literature on the anisotropic nearest and next nearest neighbor Ising model (ANNNI) [9]. This work also resulted in progress towards a quantitative understanding of their anisotropic exchange interactions [10].

A recent resurgence of interest in these rare-earth monopnictides is driven by their extreme magnetoresistance (XMR) and resistivity plateaus and the possible connection to the three-dimensional (3D) topological state of the nonmagnetic lanthanum monopnictides LaX [11,12]. LaAs, LaSb, and LaBi have unsaturated XMR arising from near perfect electron-hole compensation and there is a topological transition from a trivial electronic band structure in LaAs to a topologically nontrivial band structure in LaBi [13–17]. Several studies have confirmed the presence of protected surface states in LaBi [18–21]. Since then, extensive works have been devoted to characterizing the XMR and topological states of various RX including, for example, CeX, HoX, and PrX. XMR has been found in each reported magnetic RX with characteristics that depend on the rare-earth ion [22–30]. The stabilization of topological nontrivial electronic bands generating protected surface states was proposed for several of the magnetic monopnictides [29,31–33].

Here we study the magnetism of HoBi using modern neutron scattering techniques to gain insights into its unique magnetotransport properties [29,34]. Consistent with previous works [35–37], we confirm the antiferromagnetic (AFM) $\mathbf{k} = (\frac{1}{2}\frac{1}{2}\frac{1}{2})$ structure and the associated tetragonal lattice distortion. Due to multidomain averaging, our single-crystal neutron diffraction cannot unambiguously determine the local spin anisotropy of the $\mathbf{k} = (\frac{1}{2}\frac{1}{2}\frac{1}{2})$ AFM structure. However, we could resolve this ambiguity by measuring and modeling the magnetic excitations of HoBi, which take the form

*Corresponding author: Jonathan.Gaudet@nist.gov

 

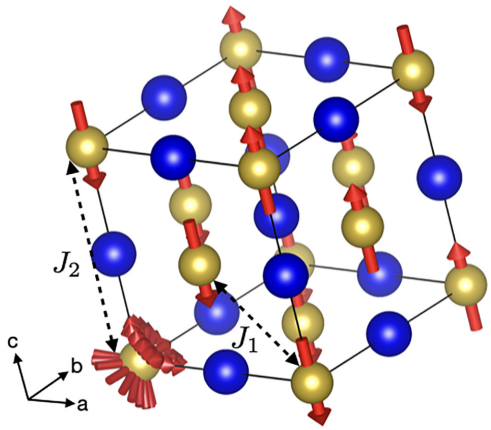


FIG. 1. Rocksalt structure of the rare-earth monopnictide HoBi. Yellow and blue spheres respectively correspond to Ho and Bi. Spins interacting through the $J_1$ and $J_2$ exchange interaction are shown by the dashed black arrows. The $\mathbf{k} = (\frac{1}{2}\frac{1}{2}\frac{1}{2})$ magnetic order of the $Ho^{3+}$ spins is represented by the red arrows. The local spin orientations of the $Ho^{3+}$ spins that are consistent with neutron diffraction are indicated for the Ho ion at (0,0,0). The magnetization, structural distortion and inelastic neutron scattering, however, provide clear evidence for easy [001] axis anisotropy.

of weakly propagating spin-orbital excitons whose energies and intensities are sensitive to the local orientation of the $Ho^{3+}$ moments. Using this method, we found the $\mathbf{k} = (\frac{1}{2}\frac{1}{2}\frac{1}{2})$ AFM structure has an Ising local spin anisotropy, which is consistent with the Ising easy-axis bulk magnetization and the tetragonal distortion. Through analysis of the paramagnetic diffuse scattering of HoBi and the crystal field excitons in the low $T$ ordered state, we obtain a spin Hamiltonian with comparable crystal field (CEF) and exchange energy scales.

## II. EXPERIMENTAL METHODS

HoBi single crystals with mass of 10–50 mg were grown following a previously published procedure [34]. Single crystal low-temperature x-ray diffraction was performed using a Huber four-circle diffractometer with a Rigaku Rotaflex 18 kW rotating copper anode x-ray generator and a Bicron point detector. We used a Ge (111) monochromator with $d_{111} = 3.266$ Å. The sample was aligned for diffraction in the $(HHL)$ plane and mounted in a closed cycle cryogenic system with a base temperature of 2.17 K.

We performed thermal neutron diffraction using the HB-1A triple-axis instrument at Oak Ridge National Laboratory. We used PG filtered 14.5 meV neutrons and collected rocking scans at all accessible magnetic and nuclear Bragg positions in the $(HHL)$ plane. Polarized neutron diffraction measurements were conducted with the triple-axis instrument BT-7 at the Center for Neutron Research (NCNR), NIST. Nuclear spin-polarized $^3He$ gas was used to polarize the incident neutron beam and to analyze the polarization of scattered neutrons [38,39]. Horizontal guide fields were present throughout the beam path to allow measurements of the spin-flip (SF) and non-spin-flip (NSF) scattering cross sections for incident neutron spins polarized parallel to momentum transfer **Q**. The flipping ratio measured at nuclear Bragg peaks was greater than 30.

Cold neutron triple-axis experiments were performed using the SPINS and the MACS spectrometers at the NCNR. On both instruments we employed a fixed final neutron energy $E_f = 3.7$ meV or 5 meV and measured the elastic and inelastic scattering for a single crystal of HoBi aligned for scattering within the $(HHL)$ and the $(HK0)$ plane in two different experiments. For the $E_f = 3.7$ meV configuration, we used polycrystalline cooled Be and BeO filters before and after the sample, respectively. For the 5 meV configuration we only used a Be filter after the sample, while the incident beam from the cold neutron source was unfiltered. For both experiments, we comounted 11 HoBi single crystals on an aluminum mount. We acquired background data using an identical mount without HoBi crystals. We used an "orange" 4He flow cryostat to reach a base temperature of 1.6 K for these experiments.

For the highest energy resolution and energy transfer, we performed time-of-flight neutron scattering experiments using the CNCS spectrometer at Oak Ridge National Laboratory. There we coaligned two HoBi single crystals on an aluminum mount and collected inelastic neutron scattering data with fixed incident energy $E_i = 25$ meV at $T = 13$ K with a total proton charge of 47 C. We used the high flux mode of operation of CNCS with a Fermi Chopper, Chopper 2, Chopper 3, and a Double Disk frequency of 60, 60, 60, 300, and 300 Hz, respectively. The energy resolution (FWHM) at the elastic line for this configuration is 2.0(1) meV. Finally, we note that the error bars associated with the neutron scattering experiments represent one standard deviation.

Both the magnetization and heat capacity measurements presented here were performed in a Quantum Design physical properties measurement system (PPMS). We used a PPMS dilution refrigerator option for the low-temperature heat capacity.

## III. RESULTS AND ANALYSIS

### A. First order phase transition

The thermodynamic properties of HoBi were previously reported and a long-range $\mathbf{k} = (\frac{1}{2}\frac{1}{2}\frac{1}{2})$ antiferromagnetic (AFM) order is known to occur concomitantly with a structural distortion around $T_N = 5.7$ K [14,35,36]. The order of the transition, however, remains unknown. To determine the order of the phase transition, we measured the temperature dependent specific heat capacity using the long-pulse heat method [40]. The resulting $C_p$ data for HoBi is reported in Fig. 2 for both warming and cooling protocols. A sharp peak with a thermal hysteresis of 13(2) mK is observed in $C_p$. Correspondingly the inset shows a distinct plateau in the temperature versus time curves during heating and cooling. These observations indicate a first order phase transition at $T_N$ in HoBi.

### B. Paramagnetic phase

To determine the magnetic interactions leading to this phase transition, we mapped the neutron elastic scattering for momentum transfer **Q** covering the $(HHL)$ plane and for

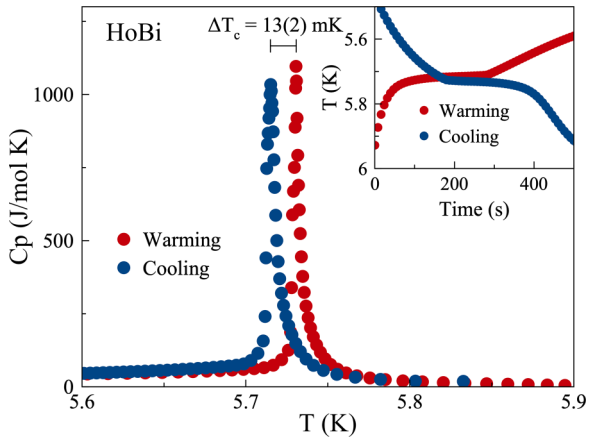


FIG. 2. Low temperature heat capacity of HoBi collected using the long-pulse method. The red and blue curves respectively correspond to the warming and cooling protocol and show a thermal hysteresis of 13(2) mK. The top inset shows the time dependence of the measured temperature upon applying a heat pulse to warm the sample temperature above $T_N$ (red curve) and upon cooling through the transition (blue curve). The observation of a plateau at $T_N$ in the heating profile for both warming and cooling protocol suggests a first order phase transition in HoBi.

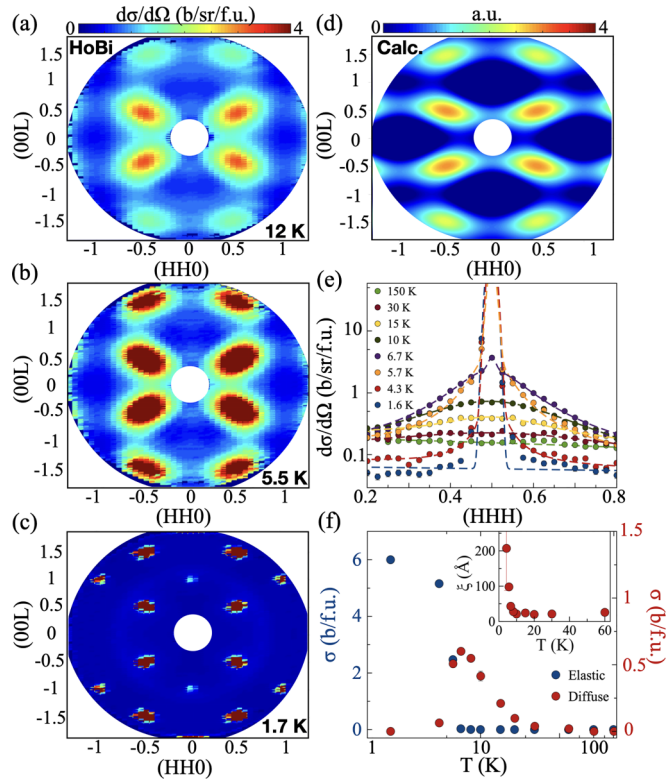


FIG. 3. Elastic diffuse neutron scattering from HoBi measured in the $(HHL)$ reciprocal lattice plane at (a) 12 K, (b) 5.5 K, and (c) 1.7 K with an incident neutrons energy of 3.7 meV. The scattering for panels (a), (b), and (c) have been symmetrized to increase statistics. (d) Calculated paramagnetic diffuse scattering with $J_1/J_2 = -2.17$ on an fcc lattice, where $J_1$ is the first NN ferromagnetic interaction and $J_2$ is the second NN antiferromagnetic interaction. Panel (e) is the elastic neutron scattering near the $\mathbf{Q} = (\frac{1}{2}\frac{1}{2}\frac{1}{2})$ Bragg peak acquired through scans along the $(HHH)$ direction. The data in panel (e) were fitted using a Lorentzian function for the diffuse scattering and a Gaussian function for the resolution limited Bragg component. The inferred integrated intensity for each component of the scattering are plotted in panel (f) as a function of temperature. The temperature dependence of the magnetic correlation length is plotted in the inset panel of (f).

temperatures between 150 K and 1.6 K. Representative data sets are shown in Fig. 3.

In the cubic paramagnetic phase for $T = 12$ K $> T_N = 5.72(1)$ K, the scattering is broad in $\mathbf{Q}$ and is centered at $\mathbf{k} = (\frac{1}{2}\frac{1}{2}\frac{1}{2})$ positions [Fig. 3(a)]. This indicates short-range AFM correlations preceding the long-range order. The "butterfly" pattern of paramagnetic diffuse scattering is consistent with the equal time structure factor $\mathcal{S}(\mathbf{Q})$ of an fcc Heisenberg paramagnet with FM interactions between the first nearest-neighbor (NN) $Ho^{3+}$ ions ($J_1$) and AFM interactions between the second NN ($J_2$). Dashed lines in Fig. 1 indicate the lattice geometry associated with these interactions. The scattered intensity was modeled using $\mathcal{I}(\mathbf{Q}) = \frac{2}{3}N|f(\mathbf{Q})|^2 \sum_{ij}\langle \mathbf{S}_i \cdot \mathbf{S}_j\rangle \cos(\mathbf{Q}\cdot\mathbf{r}_{ij})$, where $N$ is the number of spins, $\mathbf{r}_{ij}$ is the displacement vector from $Ho^{3+}$ site $j$ to $i$, and $f(\mathbf{Q})$ is the $Ho^{3+}$ atomic form factor [41]. Including only self-correlations and correlations between spins separated by $\{100\}$ and $\{\frac{1}{2}\frac{1}{2}0\}$, a ratio of $\langle \mathbf{S}_i \cdot \mathbf{S}_j\rangle_{\{100\}}/\langle \mathbf{S}_i \cdot \mathbf{S}_j\rangle_{\{\frac{1}{2}\frac{1}{2}0\}} = -2.2(2)$ was obtained at $T = 12$ K. The calculated magnetic diffuse scattering corresponding to the best fit shown in Fig. 3(d) accounts for all major features in the data [Fig. 3(a)] and the introduction of third NN correlations does not improve the fit significantly. A high temperature expansion allows us to associate the ratio of correlations to the ratio of the corresponding exchange interactions [42,43] so that we may infer that $J_2/J_1 \approx -2.2(2)$. Even if some of the $J_1$ bond interactions are frustrated, this resulting fitted ratio of exchange parameters stabilize a $\mathbf{k} = (\frac{1}{2}\frac{1}{2}\frac{1}{2})$ order, which is driven by the dominant AFM $J_2$ interactions [44–46].

Upon cooling, the elastic magnetic scattering gets stronger [$T = 5.5$ K $\approx T_N$ in Fig. 3(b)] and eventually forms magnetic Bragg peaks [$T = 1.6$ K $\ll T_N$ in Fig. 3(c)] indicating long range magnetic order. To quantify the temperature dependence of the diffuse and Bragg scattering, as shown in Fig. 3(e), we fitted the integrated intensity obtained from one-dimensional $(HHH)$ scans acquired through the magnetic Bragg peak at $\mathbf{Q} = (\frac{1}{2}\frac{1}{2}\frac{1}{2})$. Each scan was fit to the sum of a Gaussian function and a Lorentzian function to describe the long and short range components of the spin correlations and a linear background (needed to describe the temperature-independent nuclear and temperature-dependent magnetic incoherent elastic scattering). The fits included as dashed curves in Fig. 3(e) provide a good account of the data.

The temperature dependence of the integrated intensity of both the Bragg and the diffuse components of the scattering are reported in Fig. 3(f). The integrated intensity of the diffuse scattering (red markers) is peaked at $T_N$, where the appearance of Bragg scattering (blue markers) reveals the onset of long range order and translation symmetry breaking. The temperature variation of the correlation length $\xi$, as inferred from the Lorentzian after correcting for resolution effects, is reported

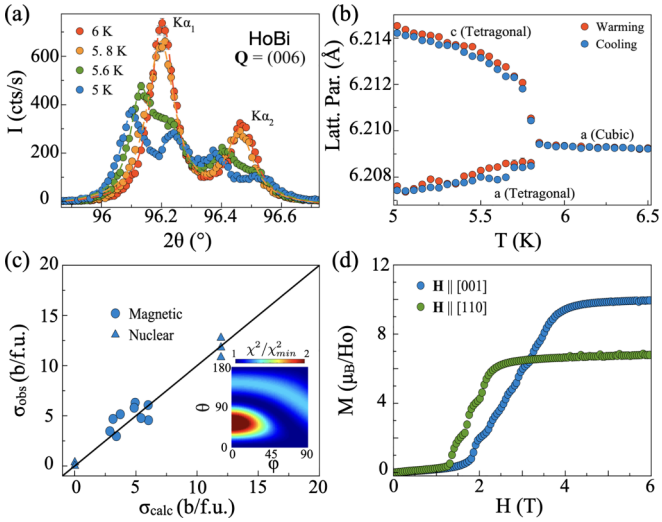


FIG. 4. Series of $\theta - 2\theta$ x-ray diffraction scans through the $\mathbf{Q} = (006)$ Bragg peak. The inferred temperature dependence of the lattice parameters is shown in panel (b). The neutron magnetic and nuclear refinement of HoBi are presented in (c) where the observed cross sections for various Bragg peaks are plotted as a function of the calculated cross sections. The inset in (c) reports the variation of the $\chi^2$ goodness of fit for the magnetic refinement of HoBi assuming a multidomain $\mathbf{k} = (\frac{1}{2}\frac{1}{2}\frac{1}{2})$ spin structure with an easy axis defined by spherical coordinates $\theta$ and $\phi$ ($\phi = 0$ corresponds to the [110] direction). Panel (d) shows the low-temperature magnetization versus field for fields applied parallel to the [001] and [110] directions. The data show that [001] is the easy axis.

in the inset of Fig. 3(f). As expected, $\xi$ increases dramatically at $T_N$.

### C. Structural distortion

A previous x-ray diffraction study revealed that a tetragonal distortion accompanies magnetic ordering in HoBi [35]. We confirmed the occurrence of this distortion in HoBi with a four-circle x-ray diffractometer experiment. The $\theta - 2\theta$ scans of various nuclear Bragg peaks were collected above and below $T_N$ with a base temperature of 5 K. Consistent with previous work [35], we observed a splitting of the $(H00)$, $(0K0)$, and $(00L)$ nuclear Bragg peaks, whereas the $(HHH)$ Bragg peaks do not split. This indicates a tetragonal distortion and specifically precludes a rhombohedral distortion.

The temperature dependence of a longitudinal $\theta - 2\theta$ scan through the $\mathbf{Q} = (006)$ peak is plotted in Fig. 4(a). This is an unfiltered copper source with $K_{\alpha 1}$ and $K_{\alpha 2}$ radiation. Both components yield a split (006) peak below $T_N$. The distortion was quantified by fitting the $\theta - 2\theta$ scans to Lorentzian functions while constraining the ratio of the $K_{\alpha 1}/K_{\alpha 2}$ integrated intensity to be temperature independent and set by its fitted value obtained at high temperatures. Examples of these fits are included in Fig. 4(a). The temperature dependent lattice parameters inferred from this analysis are shown in Fig. 4(b). The order parameter-like temperature dependence is similar for both warming and cooling with no hysteresis detected down to the 100 mK temperature scale. For comparison the hysteresis detected through heat capacity measurements was 13 mK (Fig. 2). A single (006) Bragg peak with a lattice parameter of 6.2095(1) Å above $T_N$ splits into two peaks with lattice parameters 6.2143(1) Å and 6.2075(1) Å below $T_N$. Assuming an approximately volume conserving phase transition implies that the lattice parameter that changes most is the $c$ axis. This indicates the structural unit cell elongates along the $c$ axis in the AFM state with $c/a = 1.0011(1)$ at 5 K. We note that an orthorhombic distortion with the $a$ and $b$ axis differing by less than 0.002 Å is not excluded by these data.

A possible space group for HoBi below $T_N$ is the maximal tetragonal subgroup of the paramagnetic space group $Fm\bar{3}m$, which is $I4/mmm$. The structural parameters in the tetragonal phase are $a_T = b_T = 6.2075(1)/\sqrt{2}$ Å and $c_T = 6.2143(1)$ Å, where the $\mathbf{a}_T$ and $\mathbf{b}_T$ axes are rotated by 45° relative to the $\mathbf{a}$ and $\mathbf{b}$ axes of the paramagnetic simple cubic cell. In this space group $Ho^{3+}$ ions occupy a single $2a$ Wyckoff site and the magnetic ordering vector is $\mathbf{k} = (\frac{3}{2}0\frac{3}{2})$. While we must use the tetragonal space group below $T_N$, we continue to use the cubic unit cell to index wave vector transfer in the neutron scattering experiments, which do not resolve the multidomain tetragonal distortion.

### D. Spin structure

As described in the previous sections, the magnetic order has a characteristic wave vector $\mathbf{k} = (\frac{1}{2}\frac{1}{2}\frac{1}{2})$. In addition to the corresponding low $T$ magnetic Bragg peaks, the intensities of all nuclear Bragg peaks are observed to increase below $T_N$. The increase of intensity is approximately proportional to the intensity in the paramagnetic phase, which indicates it arises from secondary extinction release [47]. To check this hypothesis, we performed polarized neutron diffraction on the (002) and (220) Bragg peaks below $T_N$ and found them to be exclusively nuclear in origin.

We note that weak $\mathbf{k} = (001)$ Bragg peaks also onset at $T_N$. Examples of these peaks include the (001) and (111) Bragg peaks [see Fig. 3(c)], which are forbidden within the $Fm\bar{3}m$ space group. These Bragg peaks are attributed to multiple magnetic scattering as their presence depends on both the employed incident neutron wavelength and the scattering plane, and they are absent in powder neutron diffraction measurements [36]. The multiple scattering processes involve magnetic $\mathbf{k} = (\frac{1}{2}\frac{1}{2}\frac{1}{2})$ Bragg reflections so they occur only for $T < T_N$.

Referring to fcc close packing, the AFM $\mathbf{k} = (\frac{1}{2}\frac{1}{2}\frac{1}{2})$ spin structure can be described as an AFM stacking of FM triangular lattices. As the magnetic order and structural distortion in HoBi occur in a single first order phase transition, the direction of the spins in each FM sheet is not constrained by the usual Landau argument for second order phase transitions. To determine the local spin orientation of the $Ho^{3+}$ ions, we collected 18 rocking scans at different magnetic Bragg positions for a sample presumed to be in an unbiased multidomain state. The data were compared to a cubic domain average of the calculated magnetic Bragg diffraction for a general spin orientation within one domain given by spherical angles $\theta$, $\phi$, and $\mathbf{k} = (\frac{1}{2}\frac{1}{2}\frac{1}{2})$. Here $\theta = 0$ corresponds to the tetragonal $c$ direction and $\theta = \pi/2$ and $\phi = 0$ correspond to the [110] direction. Minimizing with respect to the moment size at each point, the $\chi^2$ measure of fit quality is shown

versus $\theta$ and $\phi$ in the inset panel of Fig. 4(c). The manifold of states represented by the red arrows in Fig. 1 are indistinguishable by neutron diffraction. This degeneracy arises because the magnetic diffraction intensity for a multidomain sample only depends on the smallest angle between the spin and a $\langle 111 \rangle$ axis. From our refinement, we find this angle is $47(10)^\circ$. This is experimentally indistinguishable from the angle between [001] and [111], which is $55^\circ$. This means the magnetic diffraction data are consistent with spins pointing along the [001] directions, but also with many other directions including close to the [110] direction.

Fortunately the spin anisotropy of the $Ho^{3+}$ ions can be deduced from other pieces of information. First, the low-temperature magnetization of HoBi shown in Fig. 4(d) reveals the saturation magnetization is larger for fields along the [001] direction than along [110]. Second, the structural distortion also occurs along the [001] direction. Both of these measurements are consistent with spins oriented along the tetragonal $c_T$ axis in the AFM ordered state. Additionally, in Sec. III F we show that a [001] easy axis anisotropy is needed to accurately model the inelastic neutron scattering spectrum below $T_N$. We thus conclude the spins in the AFM type II order of HoBi are oriented along the $\mathbf{c}_T$ direction, which is the direction of the structural elongation. The comparison between measured and calculated magnetic Bragg intensities is shown in Fig. 4(c). The corresponding spin structure is shown in Fig. 1. An ordered moment of $10.3(6)\mu_B$ was determined, which is experimentally indistinguishable from the $gJ\mu_B = \frac{5}{4} \times 8\mu_B = 10\mu_B$ saturation magnetization of $Ho^{3+}$.

### E. Crystal electrical field interaction

For $Ho^{3+}$ ions, the $J = 8$ spin-orbit ground state manifold is $(2J + 1) = 17$ fold degenerate under full rotation symmetry. This degeneracy is, however, lifted by the symmetry breaking crystal electric fields (CEF). Using the Stevens operator formalism, the CEF Hamiltonian appropriate for $Ho^{3+}$ in the high-temperature cubic phase of HoBi can be expressed as follows:

$$\hat{H}_{\text{cef}}^{\text{cubic}} = B_4\left(\hat{O}_4^0 + 5\hat{O}_4^4\right) + B_6\left(\hat{O}_6^0 - 21\hat{O}_6^4\right). \tag{1}$$

Here $\hat{O}_n^m$ are Stevens operators [48] that can be written in terms of the spin-orbital angular momentum operators $\hat{J}_+$, $\hat{J}_-$, and $\hat{J}_z$, where $\hat{\mathbf{z}} \parallel \mathbf{c}$. The CEF parameters $B_n$ are scalars of dimension energy that dictate the strength of the different CEF terms and can be determined by fitting spectroscopic or thermomagnetic data sensitive to the crystal field level scheme. $B_n$ can also be estimated through the point-charge model [49].

Following Hutching's formalism [49] the point charge model yields

$$B_4 = \frac{7|e||q_{Bi}|\beta_J\langle r^4\rangle}{64\pi\epsilon_0 d_{Bi}^5} \tag{2}$$

and

$$B_6 = \frac{3|e||q_{Bi}|\gamma_J\langle r^6\rangle}{256\pi\epsilon_0 d_{Bi}^7}. \tag{3}$$

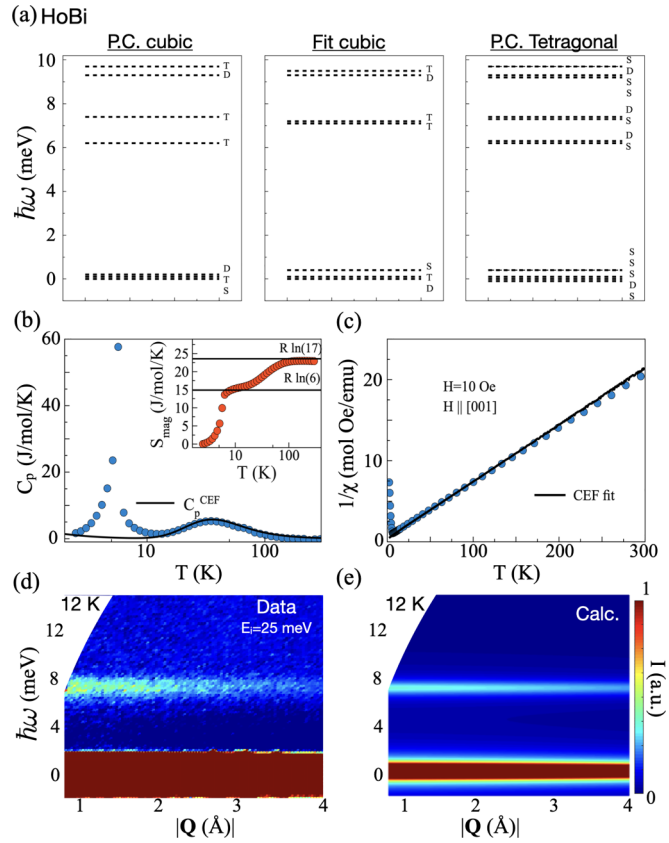


FIG. 5. Determination of the crystal electric field (CEF) level scheme for the $J = 8$ $Ho^{3+}$ ion in HoBi. Panel (a) shows the results of a point charge (PC) calculation for the cubic and tetragonal phases. The cubic CEF scheme may be compared to the level scheme for the fitted CEF Hamiltonian of HoBi. Panels (b) and (c) respectively show the temperature dependence of the magnetic heat capacity ($C_p$) and the inverse magnetic susceptibility of HoBi compared to corresponding properties based on the fitted CEF Hamiltonian. The magnetic entropy obtained from integrating the $C_p$ of HoBi is shown in the inset of (b). The measured (d) and calculated (e) inelastic neutron scattering spectra of HoBi are shown for $T = 12$ K. The neutron inelastic scattering data were acquired using a 25 meV incident neutron beam.

Here $e$ is the electron charge, $q_{Bi}$ is the charge of the Bi ligand, and $\epsilon_0$ is the vacuum permittivity. $\beta_J$ and $\gamma_J$ are reduced matrix elements calculated in Ref. [48], whereas the radial integrals for the $4f$ state $\langle r^n\rangle$ are tabulated in Ref. [50]. We used $q_{Bi} = -3e$ and the distance between a holmium ion and its first NN bismuth ion $d_{Bi} = a/2 = 6.2093(1)/2$ Å. Introducing these values in Eqs. (2) and (3) we obtain $B_4 = -2.2709(2) \times 10^{-4}$ meV and $B_6 = -1.0468(1) \times 10^{-7}$ meV.

The corresponding CEF level scheme for $Ho^{3+}$ in the cubic phase of HoBi is shown in Fig. 5(a). The $Ho^{3+}$ $J$ multiplet is split into four triplets, two doublets, and one singlet that form three groups. Group I includes one doublet, one triplet, and one singlet between 0 and 0.2 meV. Group II is formed by two triplets between 6 meV and 7 meV and group III consists of a doublet and a triplet between 9 meV and 10 meV.

The CEF Hamiltonian estimated from our point-charge calculation can reproduce the temperature dependence of the magnetic heat capacity $C_p$ [Fig. 5(b)] and magnetic susceptibility $\chi$ [Fig. 5(c)]. Obtained by integrating $C_p/T$, the temperature dependence of the entropy shown in the inset of Fig. 5(b) is informative. A first entropy plateau near 10 K is associated with the sharp $C_p$ anomaly at the phase transition to long range magnetic order. The corresponding change in entropy of $\Delta S = R \ln 6$ is that associated with the group I CEF states. The second plateau at $S = R \ln 17$ is reached at room temperature and encompasses all of the entropy associated with the three groups of crystal field levels.

For a more stringent test of the point charge model, we turn to inelastic neutron scattering. Figure 5(d) shows the 12 K inelastic neutron scattering spectrum with energy transfer ranging from 0 to 15 meV. At this temperature, the group II and III of CEF states are so scarcely populated that only CEF excitations originating from group I should be visible. No significant intrinsic broadening of the CEF excitations is observed and we note, also, that the experimental resolution is too coarse to resolve CEF levels within a group. The magnetic neutron scattering cross section associated with CEF transition from group I to II and from group I to III can be computed based on the point charge CEF Hamiltonian ($I_{mn} \propto \sum_i |\langle m|J_i|n\rangle|^2$). This calculation predicts the cross section for transitions from group I to group II is 250 times stronger than for transitions from group I to group III. The intensity of the transition from I to III is thus predicted to be too weak to be detected. This explains why Fig. 5(d) shows just a single peak that we associate with transitions from group I to group II crystal field levels.

While the measured 7.2 meV gap between group I and group II CEF levels is just 0.4 meV off from the point charge prediction of 6.8 meV, we can improve our estimate of the CEF Hamiltonian by simultaneously fitting $B_4$ and $B_6$ for the best possible account of the neutron scattering spectra [Fig. 5(d)], the specific heat data [Fig. 5(b)], and the magnetic susceptibility data [Fig. 5(c)]. The best fit parameters thus obtained are $B_4 = -2.24(1) \times 10^{-4}$ meV and $B_6 = -2.4(1) \times 10^{-7}$ meV and with them the CEF Hamiltonian provides an excellent account of all single ion properties that we have measured, as shown in Fig. 5. We also note that the calculated single-ion magnetic susceptibility ($\chi$) of the $Ho^{3+}$ ions has an Ising spin anisotropy at low temperatures with $\chi_{[001]}/\chi_{[110]} = 1.53$ at $T = 10$ K. This further validates the [001] spin anisotropy of the AFM order in HoBi.

The CEF scheme obtained from our fit [Fig. 5(a)] is remarkably similar to the point-charge calculation. Also a re-scaling of our CEF Hamiltonian for HoBi using Eq. (2) and Eq. (3) considering only the different ligand spacing successfully predicts the level scheme for HoN [51]. This is in contrast with the praseodymium case where a pnictide ligand charge of $q = -2e$ is needed to bring the point charge model into agreement with experimental data [5]. This indicates that holmium monopnictides are more ionic than praseodymium monopnictides.

Finally, we estimated the effect of the tetragonal distortion on the CEF interaction in HoBi. We performed a point-charge calculation assuming that the first NN Ho-Bi bond is shorter along the **a** and **b** direction ($d_a$) as compared to the **c** direction ($d_c$). The calculated CEF Hamiltonian can be written as

$$\mathcal{H}_{\text{cef}}^{\text{tet}} = \frac{|e||q_{Bi}|}{4\pi\epsilon_0}\left\{\alpha_J\langle r^2\rangle\left(\frac{1}{d_c^3} - \frac{1}{d_a^3}\right)\hat{O}_2^0 + \beta_J\langle r^4\rangle\left[\left(\frac{1}{4d_c^5} + \frac{3}{16d_a^5}\right)\hat{O}_4^0 + \frac{35}{16d_a^5}\hat{O}_4^4\right] + \gamma_J\langle r^6\rangle\left[\left(\frac{1}{8d_c^7} - \frac{5}{64d_a^7}\right)\hat{O}_6^0 - \frac{63}{64d_a^7}\hat{O}_6^4\right]\right\}. \quad (4)$$

The corresponding level scheme is shown in Fig. 5(a). For this calculation, we used the lattice parameters determined in our high-resolution x-ray scattering experiment. The degeneracy of all the triplets and doublets associated with cubic symmetry is lifted. This results in four doublets and nine singlets and a significant broadening of each of the three groups of crystal field levels.

### F. Low energy spin dynamics

We now turn our attention to the collective physics of HoBi, which we explore using inelastic magnetic neutron scattering. Figure 6(a) shows the temperature dependence of the inelastic scattering for $\mathbf{Q} = (\frac{1}{2}\frac{1}{2}\frac{1}{2})$. Just above $T_N$, the scattering is quasielastic with a physical (resolution corrected) FWHM of 0.30(5) meV. No inelastic intensity is observed up to 2 meV. This is consistent with the CEF energy scheme shown in Fig. 5(c). Below $T_N$, the quasielastic scattering splits into an elastic and an inelastic component.

To probe any dispersion of the low energy spin excitations, we acquired low energy spectra at momentum transfer **Q** corresponding to high symmetry points in the Brillouin zone. Figure 6(b) shows the spectrum consists of a peak that is broader than the experimental resolution (FWHM indicated by horizontal bar) and that shifts by less than the peak width between the different values of **Q**. A Gaussian fit finds the peak centered at 1.7(2) meV with a FWHM of 0.48(4) meV that exceeds the instrumental resolution (FWHM of 0.22 meV). The limited resolution and statistical accuracy of the data does not rule out the possibility of multiple dispersive components within the approximately Gaussian envelope of the peak.

We also examined the higher energy excitations for $T < T_N$ by acquiring momentum resolved inelastic scattering data up to 11.5 meV. A representative slice through the data is displayed as a color image versus **Q** along the $(HH0)$ direction and energy transfer in Fig. 6(c). No dispersion is resolved. The data are similar to the high-temperature plot of intensity versus $|Q|$ and $\hbar\omega$ in Fig. 5(d) though with additional inelastic features at 9.0(3) meV and 1.7(2) meV.

Figure 6(e) shows the momentum dependence of the integrated intensity of the 1.7 meV mode throughout the $(HHL)$ zone. The **Q** dependence of the intensity is subtle albeit peaked at the magnetic $(\frac{1}{2}\frac{1}{2}\frac{1}{2})$ zone center and smoothly decreases with $|Q|$ in accordance with the $Ho^{3+}$ magnetic form factor [41]. We note that the 1.7 meV gap is about an order of magnitude greater than the predicted CEF gap arising from the tetragonal distortion. This indicates the phase transition is driven by the magnetic interactions, which we model below.

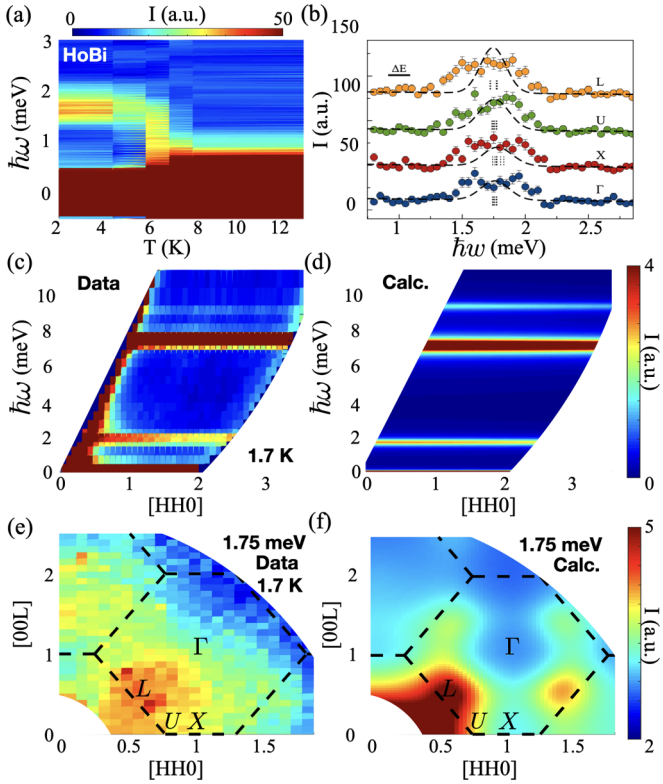


FIG. 6. Temperature dependence of the low energy inelastic neutron spectrum of HoBi at $\mathbf{Q} = (\frac{1}{2}\frac{1}{2}\frac{1}{2})$ is shown in panel (a). The spectrum of neutron scattering at some high symmetry positions within the first Brillouin zone of HoBi are shown in (b).The horizontal black bar indicates the FWHM energy resolution of the spectrometer, while the black dashed lines show the predicted spectrum based on the spin Hamiltonian presented in this work. The energies associated with each exciton are indicated by vertical black dashed lines. The observed and calculated inelastic neutron scattering spectrum up to 11.5 meV are respectively plotted in (c) and (d) for momentum transfer $\mathbf{Q}$ along the $[HH0]$ direction. The observed and calculated momentum dependence of the 1.75 meV exciton scattering intensity is shown in (e) and (f). The energy integration for panel (e) is $\pm 0.25$ meV.

## IV. MODELING SPIN DYNAMICS OF SPIN-ORBITAL EXCITONS

The low-temperature excitations in HoBi are similar to other rare-earth metallic compounds where exchange interactions are strong enough to mix crystal field levels [4,52,53]. Because components that are longitudinal with respect to the ordered moment are involved, these are not conventional transverse spin wave excitations. They may be described as crystal field excitations that can propagate through the lattice due to intersite interactions. We shall adopt the practice of calling these "crystal field exciton" or simply "exciton" [54–56].

A common theoretical approach to describing excitons in rare-earth magnets is to use a pseudoboson theory where the exciton creation operator is a linear combination of single-ion operators [53,57,58]. In this theory, the $\mathbf{Q} = \mathbf{0}$ single-ion operators are obtained by diagonalizing the mean-field spin Hamiltonian and the dispersion at finite $\mathbf{Q}$ is produced by the exchange terms. We use this pseudoboson theory to describe the magnetic excitation spectrum of HoBi below $T_N$. The Hamiltonian $\mathcal{H}_s$ includes the single-ion tetragonal crystal field terms and isotropic exchange interactions. $\mathcal{H}_s$ is decomposed into a mean-field term ($\mathcal{H}_{0,k}$) and an interacting part ($\mathcal{H}_{\rm int}$) so $\mathcal{H}_s = \sum_k \mathcal{H}_{0,k} + \mathcal{H}_{\rm int}$, where

$$\mathcal{H}_{0,k} = \mathcal{H}^{\rm tet}_{{\rm cef},k} + (-1)^k H_z J^k_{jz} \tag{5}$$

and

$$\mathcal{H}_{\rm int} = \sum_{j,j',k,k'} \mathcal{J}^{k,k'}_{j,j'} \mathbf{J}^k_j \cdot \mathbf{J}^{k'}_{j'} - \sum_{j,k} (-1)^k H_z J^k_{jz}. \tag{6}$$

Here $j$ indexes the unit cell, while $k = 1, 2$ specifies the antiparallel sublattices of the AFM order (Fig. 1). We define $H_z = 2\sum_r Z_r \mathcal{J}_r \langle J_z \rangle$, where $\mathcal{J}_r$ and $Z_r$ are respectively the exchange constant and coordination number associated with the $r$th neighbor. $\langle J_z \rangle$ is the thermal average of $J_z$ on each site, which we constrained to $\langle J_z \rangle = 8$ since we found from our neutron diffraction experiment that the $Ho^{3+}$ ions achieve their full saturation moment within the ordered state ($10\mu_B$). By definition, $\mathcal{H}_{\rm int}$ carries no mean value and so can be written in terms of creation ($\hat{a}^\dagger_{n,k} = |n,k\rangle\langle 0,k|$) and annihilation ($\hat{a}_{n,k} = |0,k\rangle\langle n,k|$) operators that connect the ground state $|0,k\rangle$ and the excited eigenstates $|n,k\rangle$ of $\hat{H}_{0,k}$. In this case, $\hat{H}_{0,k} = \sum_n E_n \hat{a}^\dagger_{n,k}\hat{a}_{n,k}$, where $E_{n,k}$ is the eigenvalue of the $|n,k\rangle$ eigenstate of $\hat{H}_{o,k}$. After writing $\hat{H}_s$ in terms of these operators and Fourier transforming it, we obtain

$$\hat{H}_s = \frac{1}{2}\sum_{\mathbf{Q}} \{\hat{a}^\dagger(\mathbf{Q}) A(\mathbf{Q}) \hat{a}(\mathbf{Q}) + \hat{a}^\dagger(-\mathbf{Q}) A(-\mathbf{Q}) \hat{a}(-\mathbf{Q}) + \hat{a}^\dagger(\mathbf{Q}) B(\mathbf{Q}) \hat{a}^\dagger(-\mathbf{Q}) + \hat{a}(-\mathbf{Q}) B(\mathbf{Q}) \hat{a}(-\mathbf{Q})\}, \tag{7}$$

with $\hat{A} = \hat{\Delta} + 2\hat{h}_{zz} + \hat{h}_{+-} + \hat{h}_{-+}$ and $\hat{B} = 2\hat{h}_{zz} + \hat{h}_{++} + h_{--}$, where $\hat{\Delta} = E_{n,k}\delta_{k,k'}\delta_{n,n'}$ and $\hat{h}_{\alpha\beta}(k,k',n,n',\mathbf{Q}) = J(\mathbf{Q})\langle k,n|\hat{J}_\alpha|0,k\rangle\langle k',0|\hat{J}_\beta|n',k'\rangle$.

The procedure to compute the spin dynamics first consists of diagonalizing $\hat{H}_{0,k}$ to obtain the eigenvalues $E_{n,k}$ and eigenvectors $|n,k\rangle$ for $\mathbf{Q} = \mathbf{0}$. At finite $\mathbf{Q}$, the matrix $\hat{H}_s = \begin{pmatrix} \hat{A} & \hat{B} \\ -\hat{B} & -\hat{A} \end{pmatrix}$ is then computed and diagonalized to obtain the perturbed energies $[E_{\tilde{n}}(\mathbf{Q})]$ and eigenstates $|\tilde{n}(\mathbf{Q})\rangle$ for each exciton. We consider all the excited CEF states belonging to the $(2J+1)$ spin-orbit manifold of HoBi so there are 32 creation and annihilation operators for each of the two $Ho^{3+}$ spins within the magnetic unit cell. This gives a Hilbert space of 64 states for $\hat{H}_s$. The associated inelastic magnetic neutron scattering cross section for a single magnetic domain is then [53,57]

$$\frac{d^2\sigma}{dE\,d\Omega} = N(\gamma r_0)^2 \frac{k_f}{k_i} \left| \frac{g}{2} f(\mathbf{Q}) \right|^2 \times \sum_{\tilde{n},\mathbf{q},\tau_{\mathbf{m}}} |\langle \tilde{n}(\mathbf{q}) | \hat{J}_{\mathbf{Q}} | GS \rangle|^2 \delta(E - E_{\tilde{n}}(\mathbf{q})) \times \Delta(\mathbf{Q} - \mathbf{q} - \tau_{\mathbf{m}}). \tag{8}$$

Here $N$ is the number of primitive magnetic unit cells, $\gamma = -1.91$ is the gyromagnetic ratio of the neutron, $r_0 = 2.818 \times$

$10^{-15}$ m is the classical electron radius, $\tau_{\mathbf{m}}$ is the magnetic zone center, and $\mathbf{q}$ is the reduced momentum transfer within the first magnetic Brillouin zone, while $k_f$ and $k_i$ respectively are the scattered and incoming neutron wave vectors. The measured spectrum is subject to the finite resolution of the instrument which we account for by replacing the delta functions by a united normalized Gaussian function with the $\mathbf{Q}$-integrated energy resolution width. The final calculated spectrum was averaged over all possible magnetic domains.

## V. MICROSCOPIC SPIN HAMILTONIAN FOR HOLMIUM BISMUTH

We determined the microscopic parameters of $\hat{H}_s$ for HoBi by fitting the $\mathbf{Q} = \mathbf{0}$ spectrum consisting of three excitons at $E_1 = 1.7(2)$ meV, $E_2 = 7.4(2)$ meV, and $E_3 = 9.0(3)$ meV with relative intensities $I_2/I_1 = 5.5(3)$ and $I_2/I_3 = 37(7)$. Employing the ratio $\|J_2/J_1\| = 2.17$ obtained by analyzing the magnetic diffuse scattering (Sec. III B) leaves just one free parameter for the exchange interactions. A 66 times bigger $\chi^2$ is obtained by fitting the excitons using the paramagnetic cubic CEF Hamiltonian as opposed to considering the tetragonal distortion. The tetragonal CEF Hamiltonian has six free parameters that were initially estimated from the point-charge model. To reproduce the exact energies of the excitons at $E_2$ and $E_3$, we allowed the CEF parameters to relax away from their point-charge values which results in many combinations of parameters consistent with the data. We estimated the exchange constants by varying the CEF parameters away from their point-charge calculation values and keeping all solutions that have a $\chi^2$ within 20% $(1/N_{\text{obs}})$ of the global minimum. The exchange parameters refined to $J_1 = -1.4(2)$ μeV and $J_2 = 3.0(5)$ μeV. A mean-field critical temperature of 20(7) K is obtained from these parameters. For comparison, the actual ordering temperature is only $T_N = 5.72(1)$ K, but we note that the mean-field critical temperature corresponds to the temperature at which short-range correlations onset [see Fig. 3(f)]. We hypothesize that fluctuations arising from competition between the ferromagnetic $J_1$ and the antiferromagnetic $J_2$ interactions lead to the reduced critical temperature.

The right column of Fig. 6 compares the optimized model for a multidomain sample to the experimental data. Figure 6(d) shows the full intensity versus $\hbar\omega$ and $\mathbf{Q} \parallel (HH0)$ for comparison with Fig. 6(c). The position and relative intensity of the three modes are well reproduced. Looking more closely at the 1.75 meV mode, Fig. 6(b) compares the intensity versus energy transfer at select high symmetry points in the Brillouin zone. The vertical dashed lines show that multiple excitons contribute at each $\mathbf{Q}$. This is generally consistent with the featured spectrum observed, though there is more broadening/dispersion observed than reproduced by the model. Inclusion of anisotropic or longer range interactions might be needed to remedy this discrepancy, though data with higher energy resolution is needed to justify the greater model complexity. Figure 6(f) shows the calculated $\mathbf{Q}$-dependent integrated intensity of the 1.75 meV mode. The dominant features of the experimental result in Fig. 6(e) are reproduced, including mainly the increase of scattered intensity at the magnetic zone centers. We note the presence of phonon scattering near $\mathbf{Q} = (002)$ that may account for the discrepancy between the calculation and the experimental data at that momentum point.

## VI. DISCUSSION AND CONCLUSION

In this manuscript, we have characterized an antiferromagnetic order and the associated crystal field excitons that develop below $T_N = 5.72(1)$ K in the rare-earth monopnictide HoBi. This magnetic state is driven by strong second NN antiferromagnetic and weaker first NN ferromagnetic interactions, which we quantified via modeling of the diffuse paramagnetic and low temperature inelastic neutron scattering. The excitation spectrum is sensitive to the local orientation of the $Ho^{3+}$ ordered spins, which allowed us to establish the Ising nature of the antiferromagnetic order in HoBi that cannot be deduced from neutron diffraction of a multidomain sample. We used x-ray diffraction to provide evidence for a tetragonal structural distortion that accompanies magnetic ordering. Our CEF analysis and modeling of inelastic scattering data indicates the elongated $c$ axis coincides with the easy magnetic axis within a domain.

The magnetic excitations that we have documented here surely have significant impacts on the magnetotransport properties of HoBi [34]. For example, we found strong quasielastic neutron scattering in the paramagnetic state. The associated short range correlated spin fluctuations, which may be accompanied by short range tetragonal lattice distortions too given the non-Kramers nature of the $Ho^{3+}$, are expected to enhance the electrical resistivity above $T_N$. Below $T_N$, these gapless fluctuations are replaced by a coherent exciton at 1.7(2) meV and correspondingly the electrical resistivity is reduced by an order of magnitude upon cooling below $T_N$ [34]. The field dependence of spin-orbital excitons may be responsible for various features observed in the magnetoresistance of HoBi and more broadly in the rare-earth monopnictides [23–29].

## ACKNOWLEDGMENTS

This work was supported as part of the Institute for Quantum Matter, an Energy Frontier Research Center funded by the US Department of Energy, Office of Science, Basic Energy Sciences under Award No. DE-SC0019331. C.B. was further supported by the Gordon and Betty Moore foundation EPIQS program under Grant No. GBMF9456. The work at Boston College was supported by the US Department of Energy, Office of Basic Energy Sciences, Division of Physical Behavior of Materials under Award No. DE-SC0023124. This work was supported in part by the Natural Sciences and Engineering Research Council of Canada (NSERC). We acknowledge the support of the National Institute of Standards and Technology, U.S. Department of Commerce. Access to MACS was provided by the Center for High Resolution Neutron Scattering, a partnership between the National Institute of Standards and Technology and the National Science Foundation under Agreement No. DMR-1508249. The identification of any commercial product or trade name does not imply endorsement or recommendation by the National Institute of

Standards and Technology. A portion of this research used resources at the High Flux Isotope Reactor, a DOE Office of Science User Facility operated by the Oak Ridge National Laboratory.

[1] C.-G. Duan, R. F. Sabirianov, W. N. Mei, P. A. Dowben, S. S. Jaswal, and E.Y. Tsymbal, Electronic, magnetic and transport properties of rare-earth monopnictides, J. Phys.: Condens. Matter **19**, 315220 (2007).

[2] L. Petit, R. Tyer, Z. Szotek, W.M. Temmerman, and A. Svane, Rare earth monopnictides and monochalcogenides from first principles: Towards an electronic phase diagram of strongly correlated materials, New J. Phys. **12**, 113041 (2010).

[3] H. R. Child, M. K. Wilkinson, J. W. Cable, W. C. Koehler, and E. O. Wollan, Neutron diffraction investigation of the magnetic properties of compounds of rare-earth metals with group V anions, Phys. Rev. **131**, 922 (1963).

[4] K. C. Turberfield, L. Passell, R. J. Birgeneau, and E. Bucher, Neutron crystal-field spectroscopy in rare-earth metallic compounds, J. Appl. Phys. **42**, 1746 (1971).

[5] R. J. Birgeneau, E. Bucher, J. P. Maita, L. Passell, and K. C. Turberfield, Crystal fields and the effective-point-charge model in the rare-earth pnictides, Phys. Rev. B **8**, 5345 (1973).

[6] P. Schobinger-Papamantellos, A. Niggli, P. Fischer, E. Kaldis, and V. Hildebrandt, Magnetic ordering of rare earth monochalcogenides. I. neutron diffraction investigation of CeS, NdS, NdSe, NdTe and TbSe, J. Phys. C: Solid State Phys. **7**, 2023 (1974).

[7] P. Fischer, P. Schobinger-Papamantellos, E. Kaldis, and A. Ernst, Magnetic ordering of rare earth monochalcogenides. II. Neutron diffraction investigation of terbium sulphide, telluride and holmium telluride, J. Phys. C: Solid State Phys. **10**, 3601 (1977).

[8] H. Heer, A. Furrer, W. Halg, and O. Vogt, Neutron spectroscopy in the cerium monopnictides, J. Phys. C: Solid State Phys. **12**, 5207 (1979).

[9] W. Selke, The ANNNI model - Theoretical analysis and experimental application, Phys. Rep. **170**, 213 (1988).

[10] Q. G. Sheng and B. R. Cooper, Combined effect of hybridization and exchange Coulomb interaction on magnetic ordering in correlated-$f$-electron cerium systems, Phys. Rev. B **50**, 965 (1994).

[11] F. F. Tafti, Q. D. Gibson, S. K. Kushwaha, N. Haldolaarachchige, and R. J. Cava, Resistivity plateau and extreme magnetoresistance in lasb, Nat. Phys. **12**, 272 (2016).

[12] F. F. Tafti, Q. D. Gibson, S. Kushwaha, J. W. Krizan, N. Haldolaarachchige, and R. J. Cava, Temperature-field phase diagram of extreme magnetoresistance, Proc. Natl. Acad. Sci. USA **113**, E3475 (2016).

[13] P.-J. Guo, H.-C. Yang, B.-J. Zhang, K. Liu, and Z.-Y. Lu, Charge compensation in extremely large magnetoresistance materials LaSb and LaBi revealed by first-principles calculations, Phys. Rev. B **93**, 235142 (2016).

[14] H.-Y. Yang, T. Nummy, H. Li, S. Jaszewski, M. Abramchuk, D. S. Dessau, and F. F. Tafti, Extreme magnetoresistance in the topologically trivial lanthanum monopnictide LaAs, Phys. Rev. B **96**, 235128 (2017).

[15] R. Lou, B.-B. Fu, Q. N. Xu, P.-J. Guo, L.-Y. Kong, L.-K. Zeng, J.-Z. Ma, P. Richard, C. Fang, Y.-B. Huang, S. S. Sun, Q. Wang, L. Wang, Y.-G. Shi, H. C. Lei, K. Liu, H. M. Weng, T. Qian, H. Ding, and S.-C. Wang, Evidence of topological insulator state in the semimetal LaBi, Phys. Rev. B **95**, 115140 (2017).

[16] H. Oinuma, S. Souma, D. Takane, T. Nakamura, K. Nakayama, T. Mitsuhashi, K. Horiba, H. Kumigashira, M. Yoshida, A. Ochiai, T. Takahashi, and T. Sato, Three-dimensional band structure of LaSb and CeSb: Absence of band inversion, Phys. Rev. B **96**, 041120(R) (2017).

[17] T. J. Nummy, J. A. Waugh, S. P. Parham, Q. Liu, H.-Y. Yang, H. Li, X. Zhou, N. C. Plumb, F. F. Tafti, and D. S. Dessau, Anomalous quantum oscillations and evidence for a non-trivial Berry phase in SmSb, npj Quantum Mater. **3**, 24 (2018).

[18] X. H. Niu, D. F. Xu, Y. H. Bai, Q. Song, X. P. Shen, B. P. Xie, Z. Sun, Y. B. Huang, D. C. Peets, and D. L. Feng, Presence of exotic electronic surface states in LaBi and LaSb, Phys. Rev. B **94**, 165163 (2016).

[19] R. Singha, B. Satpati, and P. Mandal, Fermi surface topology and signature of surface dirac nodes in LaBi, Sci. Rep. **7**, 1 (2017).

[20] J. Nayak, S.-C. Wu, N. Kumar, C. Shekhar, S. Singh, J. Fink, E. E. D. Rienks, G. H. Fecher, S. S. P. Parkin, B. Yan, and C. Felser, Multiple Dirac cones at the surface of the topological metal LaBi, Nat. Commun. **8**, 13942 (2017).

[21] B. Feng, J. Cao, M. Yang, Y. Feng, S. Wu, B. Fu, M. Arita, K. Miyamoto, S. He, K. Shimada, Y. Shi, T. Okuda, and Y. Yao, Experimental observation of node-line-like surface states in LaBi, Phys. Rev. B **97**, 155153 (2018).

[22] O. Pavlosiuk, P. Swatek, D. Kaczorowski, and P. Wiśniewski, Magnetoresistance in LuBi and YBi semimetals due to nearly perfect carrier compensation, Phys. Rev. B **97**, 235132 (2018).

[23] D. D. Liang, Y. J. Wang, C. Y. Xi, W. L. Zhen, J. Yang, L. Pi, W. K. Zhu, and C. J. Zhang, Extreme magnetoresistance and Shubnikov-de Haas oscillations in ferromagnetic DySb, APL Mater. **6**, 086105 (2018).

[24] F. Wu, C. Y. Guo, M. Smidman, J. L. Zhang, and H. Q. Yuan, Large magnetoresistance and Fermi surface topology of PrSb, Phys. Rev. B **96**, 125122 (2017).

[25] L. Ye, T. Suzuki, C. R. Wicker, and J. G. Checkelsky, Extreme magnetoresistance in magnetic rare-earth monopnictides, Phys. Rev. B **97**, 081108(R) (2018).

[26] Y.-Y. Wang, H. Zhang, X.-Q. Lu, L.-L. Sun, S. Xu, Z.-Y. Lu, K. Liu, S. Zhou, and T.-L. Xia, Extremely large magnetoresistance and electronic structure of TmSb, Phys. Rev. B **97**, 085137 (2018).

[27] Y.-Y. Wang, L.-L. Sun, S. Xu, Y. Su, and T.-L. Xia, Unusual magnetotransport in holmium monoantimonide, Phys. Rev. B **98**, 045137 (2018).

[28] Y.-Y. Lyu, F. Han, Z.-L. Xiao, J. Xu, Y.-L. Wang, H.-B. Wang, J.-K. Bao, D. y. Chung, M. Li, I. Martin, U. Welp, M. G. Kanatzidis, and W.-K. Kwok, Magnetization-governed magnetoresistance anisotropy in the topological semimetal CeBi, Phys. Rev. B **100**, 180407(R) (2019).

[29] Z. M. Wu, Y. R. Ruan, F. Tang, L. Zhang, Y. Fang, J. M. Zhang, Z. D. Han, R. J. Tang, B. Qian, and X. F. Jiang, Multiple metamagnetism, extreme magnetoresistance and nontrivial topological electronic structures in the magnetic

semimetal candidate holmium monobismuthide, New J. Phys. **21**, 093063 (2019).

[30] M. M. Hosen, G. Dhakal, B. Wang, N. Poudel, B. Singh, K. Dimitri, F. Kabir, C. Sims, S. Regmi, W. Neff, A. B. Sarkar, A. Agarwal, D. Murray, F. Weickert, K. Gofryk, O. Pavlosiuk, P. Wiśniewski, D. Kaczorowski, A. Bansil, and M. Neupane, Observation of gapped state in rare-earth monopnictide HoSb, Sci. Rep. **10**, 1 (2020).

[31] M. Neupane, M. M. Hosen, I. Belopolski, N. Wakeham, K. Dimitri, Na. Dhakal, J.-X. Zhu, M. Z. Hasan, E. D. Bauer, and F. Ronning, Observation of Dirac-like semi-metallic phase in NdSb, J. Phys.: Condens. Matter **28**, 23LT02 (2016).

[32] C. Guo, C. Cao, M. Smidman, F. Wu, Y. Zhang, F. Steglich, F.-C. Zhang, and H. Yuan, Possible weyl fermions in the magnetic kondo system CeSb, npj Quantum Mater. **2**, 1 (2017).

[33] F. Wu, C. Guo, M. Smidman, J. Zhang, Y. Chen, J. Singleton, and H. Yuan, Anomalous quantum oscillations and evidence for a non-trivial Berry phase in SmSb, npj Quantum Mater. **4**, 1 (2019).

[34] H.-Y. Yang, J. Gaudet, A. A. Aczel, D. E. Graf, P. Blaha, B. D. Gaulin, and F. F. Tafti, Interplay of magnetism and transport in HoBi, Phys. Rev. B **98**, 045136 (2018).

[35] F. Hulliger, H. R. Ott, and T. Siegrist, Low temperature behaviour of HoBi, J. Less-Common Met. **96**, 263 (1984).

[36] P. Fischer, W. Hälg, and F. Hulliger, Magnetic ordering in HoBi, HoS, ErS and ErSe, Physica B+C **130**, 551 (1985).

[37] A. Fente, H. Suderow, S. Vieira, N. M. Nemes, M. García-Hernández, S. L. Bud'ko, and P. C. Canfield, Low temperature magnetic transitions of single crystal HoBi, Solid State Commun. **171**, 59 (2013).

[38] W. C. Chen, R. Erwin, J. W. McIver III, S. Watson, C. B. Fu, T. R. Gentile, J. A. Borchers, J. W. Lynn, and G. L. Jones, Applications of 3He neutron spin filters at the NCNR, Phys. B: Condens. Matter **404**, 2663 (2009).

[39] W. C. Chen, T. R. Gentile, R. Erwin, S. Watson, Q. Ye, K. L. Krycka, and B. B. Maranville, 3He spin filter based polarized neutron capability at the NIST Center for Neutron Research, J. Phys.: Conf. Ser. **528**, 012014 (2014).

[40] A. Scheie, LongHCPulse: Long-Pulse heat capacity on a quantum design PPMS, J. Low Temp. Phys. **193**, 60 (2018).

[41] M. Blume, A. J. Freeman, and R. E. Watson, Neutron magnetic form factors and x-ray atomic scattering factors for rare-earth ions, Chem. Phys. **37**, 1245 (1962).

[42] R. M. White and B. Bayne, *Quantum Theory of Magnetism* (Springer, Berlin, 1983), Vol. 1.

[43] D. Hohlwein, J.-U. Hoffmann, and R. Schneider, Magnetic interaction parameters from paramagnetic diffuse neutron scattering in MnO, Phys. Rev. B **68**, 140408(R) (2003).

[44] L. C. Bartel, Stability of f.c.c. type-2 antiferromagnetic ordering and comments on the calculation of exchange constants: Application to MnO, $\alpha$-MnS, NiO, GdP and GdAs, Solid State Commun. **11**, 55 (1972).

[45] N.-N. Sun and H.-Y. Wang, The J1-J2 model on the face-centered-cubic lattices, J. Magn. Magn. Mater. **454**, 176 (2018).

[46] P. Balla, Y. Iqbal, and K. Penc, Degenerate manifolds, helimagnets, and multi-$q$ chiral phases in the classical Heisenberg antiferromagnet on the face-centered-cubic lattice, Phys. Rev. Res. **2**, 043278 (2020).

[47] G. E. Bacon and R. D. Lowde, Secondary extinction and neutron crystallography, Acta Crystallogr. **1**, 303 (1948).

[48] K. W. H. Stevens, Matrix elements and operator equivalents connected with the magnetic properties of rare earth ions, Proc. Phys. Soc. A **65**, 209 (1952).

[49] M. T. Hutchings, Point-charge calculations of energy levels of magnetic ions in crystalline electric fields, in *Solid State Physics* (Elsevier, Amsterdam, 1964), Vol. 16, p. 227.

[50] A. J. Freeman and R. E. Watson, Theoretical investigation of some magnetic and spectroscopic properties of rare-earth ions, Phys. Rev. **127**, 2058 (1962).

[51] A. Furrer and W. Halg, Crystal-field splittings of NdN and HoN, J. Phys. C: Solid State Phys. **9**, 3499 (1976).

[52] B. D. Rainford and J. D. Houmann, Magnetic Exciton Dispersion in Praseodymium, Phys. Rev. Lett. **26**, 1254 (1971).

[53] W. J. L. Buyers, T. M. Holden, E. C. Svensson, R. A. Cowley, and M. T. Hutchings, Excitations in KCoF3. II. Theoretical, J. Phys. C: Solid State Phys. **4**, 2139 (1971).

[54] P. M. Sarte, M. Songvilay, E. Pachoud, R. A. Ewings, C. D. Frost, D. Prabhakaran, K. H. Hong, A. J. Browne, Z. Yamani, J. P. Attfield, E. E. Rodriguez, S. D. Wilson, and C. Stock, Spin-orbit excitons in CoO, Phys. Rev. B **100**, 075143 (2019).

[55] P. M. Sarte, C. Stock, B. R. Ortiz, K. H. Hong, and S. D. Wilson, Van Vleck excitons in Ca2RuO4, Phys. Rev. B **102**, 245119 (2020).

[56] B. Yuan, M. B. Stone, G.-J. Shu, F. C. Chou, X. Rao, J. P. Clancy, and Y.-J. Kim, Spin-orbit exciton in a honeycomb lattice magnet CoTiO3: Revealing a link between magnetism in $d$- and $f$-electron systems, Phys. Rev. B **102**, 134404 (2020).

[57] T. M. Holden, E. C. Svensson, W. J. L. Buyers, and O. Vogt, Magnetic excitations in terbium antimonide, Phys. Rev. B **10**, 3864 (1974).

[58] P. Bak, Magnetic Excitations in Rare Earth $Al_2$ Compounds, AIP Conf. Proc. **24**, 152 (1975).